Investigations on the Origin of Radial Distribution of Non Metallic Inclusions in ESR ingot

Abdellah Kharicha[1], Jörg C. Korp[2], Wu[1], A. Ludwig[1]
[1] Montanuniversität, Leoben, Austria
[2] Sonderstahlwerk Breitenfeld GmbH, Wartberg, Austria

Abstract

In the present paper a 2D numerical model is used to explore the possible origins of the non uniform distribution of NMI in ingot remelted with an ESR process. Experiments where performed with 3 different melting rates, ion which both ingot and electrode where analysed by an automated REM/EDX system to determine the type, the size and the distribution of the NMI. An increase of NMI concentration with melting rate was noticed. The final distribution of particles in the ingot was found to be not uniform. The NMI concentration increases with the radial position, low in centre, and large in the ingot extremity.

Introduction

The electroslag remelting has been a popular process these days for producing clean steels with improved solidification structures. Since the electroslag remelting (ESR) process has reached industrial maturity, the importance of its metallurgical tasks (desulphurisation, improvement of the ingot structure, refining, etc.) has been readjusted. Currently the focus lies on the improvement of the microscopic and macroscopic degree of purity, which in particular aims for highly pure ESR grades and large heavy forging ingots. For designing a well secured production standard it therefore makes sense - from an operational practice view point - to investigate the refining mechanisms and the behaviour of non-metallic inclusions (NMI) during the ESR process.

The topic of non-metallic inclusions in the ESR-process has been subject of many detailed investigations [1-5]. However, results and explanations drawn from these investigations are often ambiguous and sometimes contradicting. These differences are probably due to the difference in the experimental conditions (deoxidation of the electrode, slag composition, composition of the analysed material, process temperatures, etc.).

The ESR-process comprises of the following stages: liquid film and droplet formation on the immersed electrode tip, falling of the metal droplet through the slag and finally the solidification of the liquid metal pool (see Figure 1). There are metal-slag-NMI interactions in each of the three process stages which do, more or less, contribute to the final achieved degree of purity.

	Stage 1	Stage 2	Stage 3
	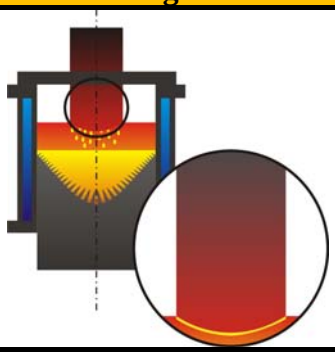	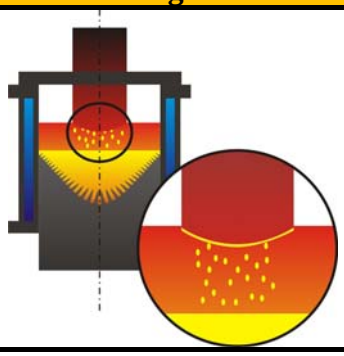	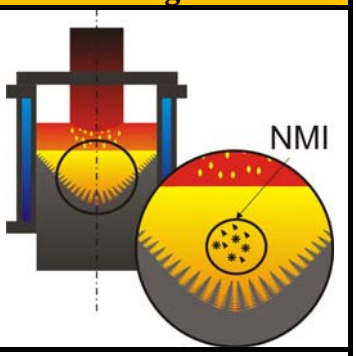
Processes	• Dissolution • Ad- resp. Absorption	• Ad- resp. Absorption	• Precipitation + Growth • Flotation

Figure 1: Refining stages in the ESR-process

Stage 1

A thin liquid metal film forms on the electrode tip when dipping the electrode into the slag. Depending on the melting rate and the slag flow its thickness is believed to be between 20 and 2500µm [1, 4, 7, 8]. In this liquefied area, the non-metallic inclusions of the electrode (e.g. deoxidation products) might begin to dissolve. A complete dissolution is unlikely since the temperature in the liquid film is only 100-150°C above its liquidus temperature. In addition the transfer time of the metal between the time when it is still solid to the time it departs with the liquid droplet is less than a second [5]. The NMI have definitively not the time to dissolve. Therefore, it is suggested that most of the non-metallic inclusions are being virtually "washed out" from the liquid metal by a mechanical phenomena. The mechanism of rejection of the NMI towards the slag/metal interface is not yet clear. However we believe that the shaking of the liquid metal film produced by the turbulent slag flow, combined with the action of the electromagnetophoretic force is enough to explain the refining at the tip of the electrode. Once an NMI is at the metal/slag interface, adsorption or absorption [9] with a subsequent dissolution within the hot slag occurs

Stage 2

Due to the low superheating of the melting metal and the very short time of 0.1-0.2s in which the droplets are in the slag [7, 8], no further dissolution of the non-metallic inclusions which still exist until then is to be expected. However, the washing out of the NMIs appears plausible since the metal within the droplets is intensively stirred during the falling. According to the work done by Zhengbang [5], a reduction in the NMI proportion was noted although it was less efficient than in stage 1.

Stage 3

The molten metal gathers in the liquid pool where the metal phase cools down until solidification begins. Dissolution reactions are not stimulated due to the decreasing temperature and decreasing dissolubility. However, precipitation and growth processes of new non-metallic inclusions and, partially, their precipitation occur.

Basically, the flotation during electroslag remelting must be scrutinised because the particles ascending velocity is extremely low in comparison to the flows due to the bath dynamic.

In [1] the comparison of samples from the liquid pool and samples from the equivalent ingot areas of the readily remelted material show that the NMI frequency in the liquid metal is slightly above the one in the remelted ingot. Mitchell [4] drew such a comparison with regard to the overall oxygen and the NMI size distribution and did not note any significant differences.

Therefore, it was suggested that flotation is possible, but does not play an important role with regard to the removal of non-metallic inclusions in ESR.

During the solidification of the liquid metal pool, new non-metallic inclusions whose size and composition is determined by the metal-NMI interactions form. The precipitation and growth of the particles mainly occur in the two-phase region between liquidus and solidus temperature [4] where segregations can be seen as a side effect of the solid/liquid transition and as impetus for the homogeneous nucleation.
In the case of a heterogeneous nucleation, non-precipitated NMI particles from the electrode would be the corresponding nucleation sites.

However, only very few inclusions get from the electrode into the pool and if this happens they are subject to an inclusion modification in the course of the process sequence [4, 12]. However, also inclusions which have been newly formed by then can act as foreign nucleus thus creating complexly built NMIs such as sulphides with an oxidic core.

Experiments

A steel X12CrNiMoV12-3 (composition see Table 1) was deoxidized with Al and cast to ESR electrodes in dyads during the rising casting process.

	C	Si	Mn	P	S	Cr	Ni	Mo	V	N
Min. %	0,08		0,40			11,00	2,00	1,50	0,25	0,020
Max. %	0,15	0,50	0,90	0,025	0,015	12,50	3,00	2,00	0,40	0,040

Table 1: Chemical composition of steel grade X12CrNiMoV12-3 (material number 1.4938)

Three electrodes were taken from one of the dyads and prepared for the subsequent processing in the electroslag remelting process (cut, sandblasting, etc.). Due to the identical derivation, it was assumed that the 3 electrodes had the same purity level. Thus only one sample from one electrode was analysed. The remelting was performed with a short collar mold under protective gas atmosphere (Figure 2**).** The slag was a standard CaF_2-CaO-Al_2O_2 slag with proportions of 3% SiO_2 and traces of MgO. The electrodes were remelted into a 7,5t ingot with Ø750mm.

Technical data

- Fixed collar mold with retraceable baseplate
- 2 electrode arms, 1 melting unit
- Protective gas (Ar or N_2)
- 30kA max. melting current
- 112V max. voltage
- 50Hz frequency
- Ingot dimension: Ø500, Ø750, Ø1000, Ø1200 ingot weight up to 33,5t as well as ingot length up to 4000mm

Figure 2: Plant characteristics and main technical data of the ESR-plant in Breitenfeld, Austria

The 3 electrodes were remelted at three different melt rates. The second electrode was remelted at the usual standard melt rate (SMR), the first and the third were remelted at 100kg/h below and 100kh/h above the standard meltrate. After having achieved and maintained the given target melting rates, solid tungsten granulates were thrown to mark the liquid pool. This was done one time through a blind hole in the electrode and one time by hand. After the end of the process, samples were taken from the ingot along the marked pool profile and analysed by means of the automated REM/EDX analysis according to the method at the voestalpine Stahl Linz [13].

Simulations

Mass and momentum conservation for an incompressible fluid are given by

$$\nabla \cdot \vec{u} = 0 \tag{1}$$

$$\rho\left[\frac{\partial \vec{u}}{\partial t} + (\vec{u} \cdot \nabla)\vec{u}\right] = -\nabla p + \mu_{eff}\nabla^2\vec{u} + \vec{F} + \vec{F}_L + \rho\beta(T - T_{ref})\vec{g} - \frac{\mu_{eff}}{\Pi}(\vec{u} - \vec{u}_{Pool}) \tag{2}$$

where $\mu_{eff} = \mu_0 + \mu_t$ is the effective viscosity due to turbulence, for which the standard k-ε model is used. μ_0 is the dynamic viscosity of the melt, ρ is the melt density, $\vec{u}$ is its mean velocity vector, p is the static pressure, $\vec{F}_L$ is the Lorentz force and $\vec{F}$ is a momentum source term which accounts for the presence of inclusions as shown in Eq. (9). The electromagnetic field is calculated with the well known potential formulation for the electric potential and magnetic potential field. Solidification within the ingot is modeled with the porosity enthalpy method. The permeability is considered by using the Black-Kozeny law. The turbulent viscosity, μ_t, is defined by

$$\mu_t = \rho C_\mu \frac{k^2}{\varepsilon} \tag{3}$$

with C_μ = 0.09. In the k-ε turbulence model the time-averaged velocity field is solved together with equations for the transport of turbulent kinetic energy, k, and its dissipation, ε,

$$\frac{\partial(\rho k)}{\partial t} + \rho\vec{u}\nabla k = \nabla\left[\left(\mu_0 + \frac{\mu_t}{\sigma_k}\right)\nabla k\right] + G_k - \rho\varepsilon\,, \tag{4}$$

$$\frac{\partial(\rho \varepsilon)}{\partial t} + \rho\vec{u}\nabla \varepsilon = \nabla\left[\left(\mu_0 + \frac{\mu_t}{\sigma_\varepsilon}\right)\nabla \varepsilon\right] + C_{1\varepsilon}\frac{\varepsilon}{k}G_k - C_{2\varepsilon}\rho\frac{\varepsilon^2}{k}\,. \tag{5}$$

In these equations, G_k represents the generation of turbulence kinetic energy due to the mean velocity gradients and $C_{1\varepsilon}$, $C_{2\varepsilon}$, and $C_{3\varepsilon}$ are constants [17]. σ_k and σ_ε are the turbulent Prandtl numbers for k and ε, respectively.

Inclusions are considered as a discrete secondary phase with spherical geometry distributed in the melt. The trajectories of these discrete phases are computed by integrating the following equation of motion in a Lagrangian frame of reference

$$\frac{d\vec{u}_p}{dt} = \frac{18\mu_0}{\rho_p d_p^2}\frac{C_D\,\mathrm{Re}}{24}\left[(\vec{u}+\vec{u}') - \vec{u}_p\right] + \frac{\vec{g}\cdot(\rho_p - \rho)}{\rho_p} - \frac{3}{4\rho_p}\vec{F}_L\,. \tag{6}$$

Here, $\vec{u}_p$ is the velocity vector, d_p the diameter and ρ_p the density of the considered discrete phase. $\vec{g}$ is the gravity vector and $\vec{u}'$ is the vector of the fluctuating velocity components defined in Eq. 11. The trajectory of an individual discrete object is based on the forces acting as it moves through the flow. The terms on the right-hand side of Eq. 6 represent the drag force, the buoyancy force and the Lorentz force. The effective Lorentz force is acting in the opposite direction than the normal Lorentz force acting on the surrounding liquid. This can be considered as a paradox as no current is flowing within the insulating inclusion. The existence of this force results from the balance of the static pressure force induced by the deviation of the current around the droplet volume. Thus when the molten metal containing non-metallic particles is put into electromagnetic field, nonconductive inclusions could move in the direction against the Lorentz force.

For the drag coefficient, C_D, the following approach is taken [18]

$$C_D = a_1 + \frac{a_2}{\mathrm{Re}} + \frac{a_3}{\mathrm{Re}^2}\,. \tag{7}$$

Here, a_1, a_2 and a_3 are constants that apply to smooth spherical inclusions over several ranges of Re. The relative Reynolds number, Re, is defined as

$$\mathrm{Re} = \frac{\rho d_p\left|\vec{u}_p - \vec{u}\right|}{\mu_0}\,. \tag{8}$$

The momentum transfer from the discrete phases to the melt is computed by examining their momentum change as

$$\vec{F} = \sum_{i}^{N} \frac{18\mu_0 C_D \,\mathrm{Re}}{\rho_p d_p^2 24}(\vec{u}_p - \vec{u})\dot{m}_p \Delta t \ . \tag{9}$$

Here, N is the number of inclusions in a computational cell and $\dot{m}_p$ is the mass flow rate of inclusions.

The dispersion of the inclusions due to turbulence in the melt is treated using a stochastic tracking model. This stochastic tracking model includes the impact of instantaneous turbulent velocity fluctuations, $u'(t)$, on the trajectories. The fluctuating velocity components are discrete piecewise constant functions of time. Their random value is kept constant over an interval of time given by the rotation time of an eddy. This rotation time, τ_e, which describes the time a inclusion/bubble spent in the turbulent motion of the considered eddy, is proportional to the discrete phase dispersion rate. Larger values indicate more turbulent motion in the flow. For the k-ε model the rotation time can be expressed according to [19] as

$$\tau_e \approx 0.3 \cdot k / \varepsilon \ . \tag{10}$$

The values of the fluctuations in 3-dimension u', v' and w' that prevail during the lifetime of the turbulent eddy are sampled by assuming that they obey a Gaussian probability distribution, so that

$$u' = \varsigma\sqrt{\frac{2k}{3}} \qquad v' = \varsigma\sqrt{\frac{2k}{3}} \qquad w' = \varsigma\sqrt{\frac{2k}{3}} \tag{11}$$

where ζ is a normally distributed random number. The discrete phase crossing time is defined as

$$t_{cross} = -\tau \cdot \ln\left[1 - \left(\frac{L_e}{\tau \cdot |u - u_p|}\right)\right] \tag{12}$$

where τ is the discrete phase relaxation time and L_e is the eddy length scale. The inclusion/bubble is assumed to interact with the melt eddy over the smaller of the eddy rotation time and the eddy crossing time. When this time limit is reached, a new value of the instantaneous velocity is obtained by applying a new value of ζ in Eq. (11).

During solidification inclusions form in the residual liquid steel due to rejection of solute elements by the solidifying dendrites (microsegregation) .Depending upon the thermodynamic conditions, segregated elements can be transported towards the liquid region and may react amongst them and may give rise to various inclusions (oxides and sulfides). Inclusions that form in regions where more than 10% of the liquid has already solidied are assumed to not be able to move. These inclusions would definitively be present within the final ingot. Therefore we focus on the trajectories of the inclusions generated close to the dendrites tips. The inclusions are assumed to nucleate uniformly between the lines 0.01 and 0.1 solid fractions.

slag height	150	mm
Mould diameter	750	mm
Electrode diameter	500	mm
Slag density	2750	mm
Slag viscosity	0.0025	mm
Metal dynamic viscosity	0.006	kg/(m s)
Liquid metal density	6900	kg/m³
gravity acceleration	9.81	m/s²
inclusion density	3800	kg/m³
inclusion diameter	2 and 9	µm

Table 1: Considered geometrical and process parameters

Since the inclusions are assumed to not influence the flow, so the particles dynamic and the liquid flow are uncoupled. Uncoupled means that the influence of the fluid flow on the movement of inclusions is considered but not the opposite.

Results

During the automated REM/EDX analysis, an area of 100mm^2 is scanned and the particles defined therein are recorded to chemical composition, size, form and position. Concerning a matrix correction, the categorisation in exactly defined inclusion classes was carried out afterwards. The data collection obtained in this way was the basis for the following evaluations.

The appearance of non-metallic inclusions in the remelted material depends on the remelting conditions, in particular on the melting rate. In order to demonstrate this influence, the total area of all inclusions per mm^2 of all NMIs is presented in Figure **3** including the average equivalent diameter and the overall oxygen content over the tested ingot areas.
As shown, the increase of the melting rate results in an increase of the NMI area proportion (B=106µm^2/mm^2 => M=110µm^2/mm^2 => S=150µm^2/mm^2). When contrasting bottom and top, the 200kg/h higher melting rate results in a NMI area increased by one and a half times. By analogy, the overall oxygen also increases (average values: $[O]_{bottom}$ =18±1ppm, $[O]_{middle}$=24±1ppm, $[O]_{top}$=29±1ppm).
Analysis in the radial direction shows that the number of inclusions area increases from the centre to ingot surface. This observation can be made for the three different melting rates. Many small particles lead to the greater NMI total areas at the boundary and less large particles to the smaller NMI areas in the centre.

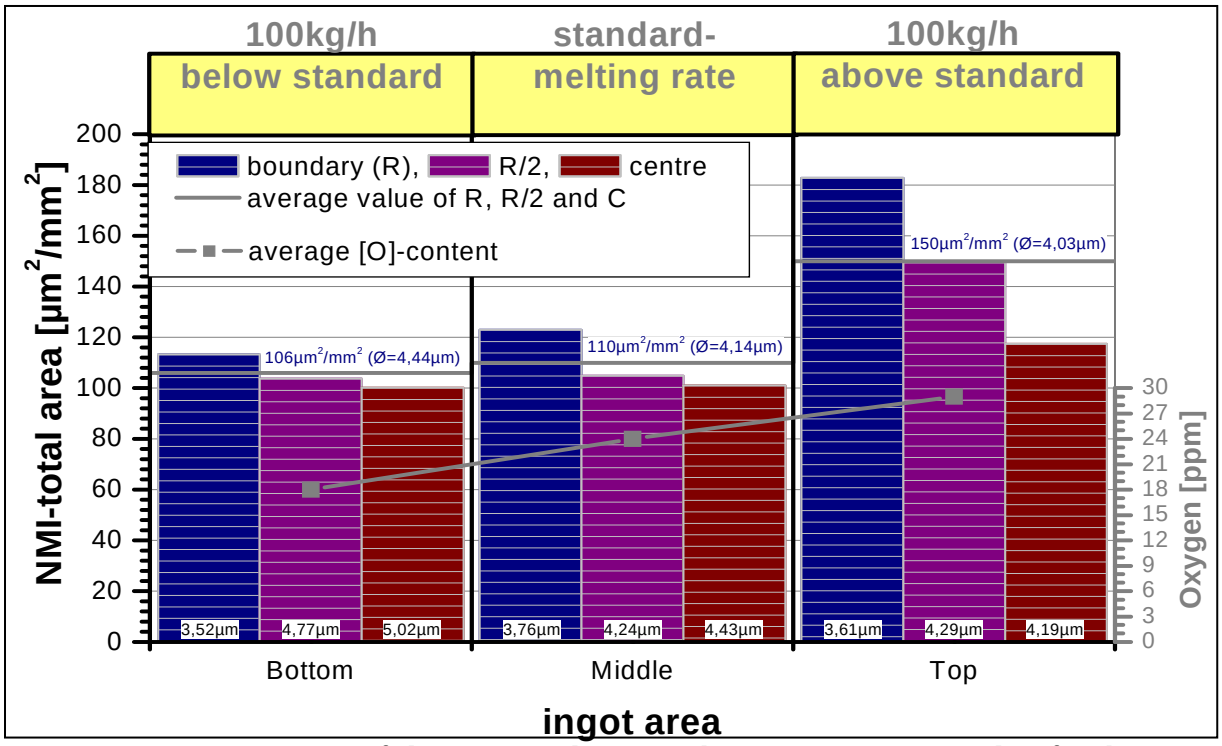

Figure 3: Comparison of the NMI-total area at the position R, R/2 and C for the ingot area bottom, middle and top

The size distribution of the dominating inclusion classes Al_2O_3 and OS are presented in **Figure 4**. As shown, the most frequent inclusion size is 3-5µm with Al_2O_3 NMIs showing their frequency maximum with 4-5µm and the oxysulphides rather below with 3-4µm. Here and there are also large particles with an equivalent diameter of >13µm. In contrast to that, the largest Al_2O_3 inclusions shown in the experiment measured 12µm. The average particle size increases from the boundary towards the centre. This is, for instance, the case with the Al_2O_3 classes at the bottom where the particle diameter of 3.8µm at the boundary increases to 5.6µm in the centre.

The particle frequency increases with the melting rate from the bottom to the top. There were 1379 Al_2O_3 and OS inclusions per cm^2 when the melting rate was low in the beginning and almost twice as much with 2656$NMIs_{(Al2O3+OS)}/cm^2$ at the highest melting rate at the end of the process.

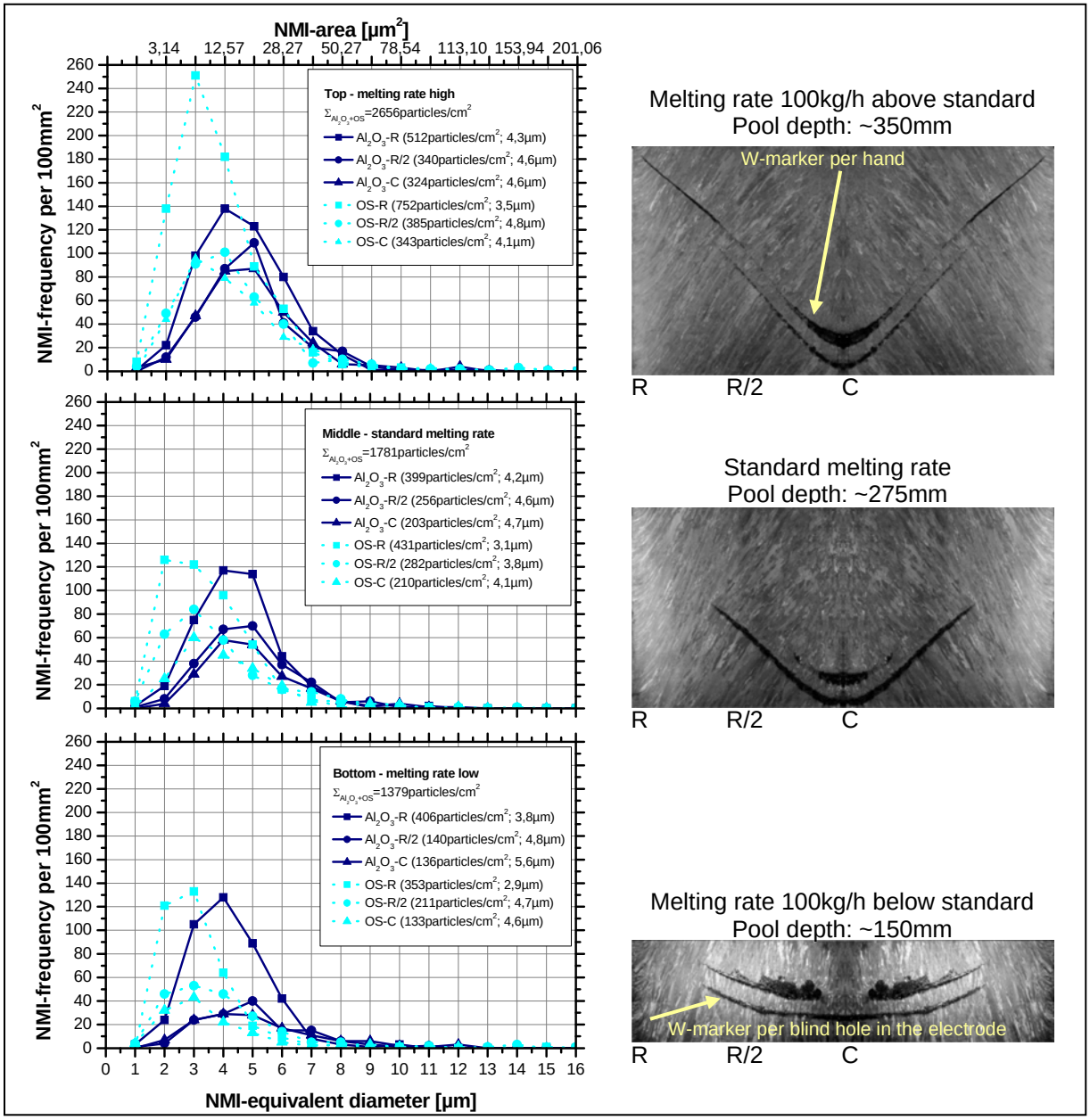

Figure 4: Al_2O_3 and Oxisulphides size distributions at the position Radius, Radius/2 and Center for ingot area bottom, middle and top

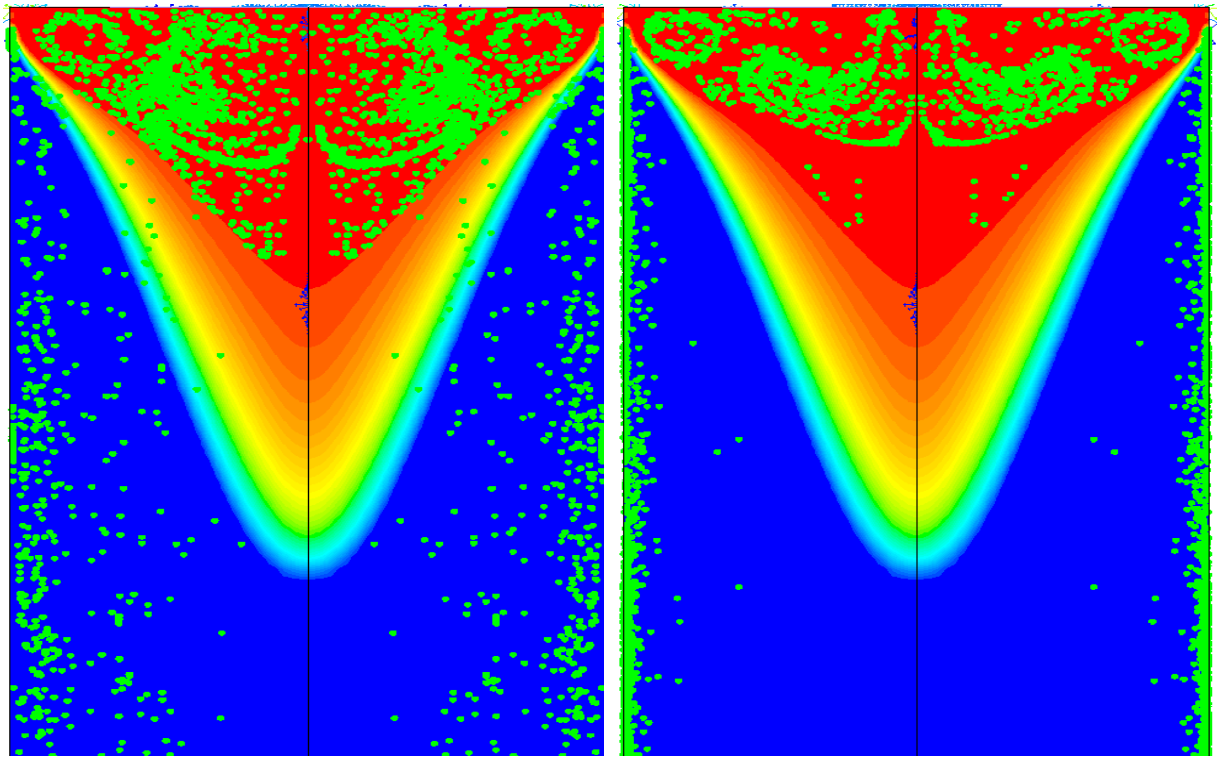

2 μm 9 μm

Figure 5: Distribution of inclusions (green dots) in the solidifying ingot. Liquid fraction 0(Blue) - 1(red).

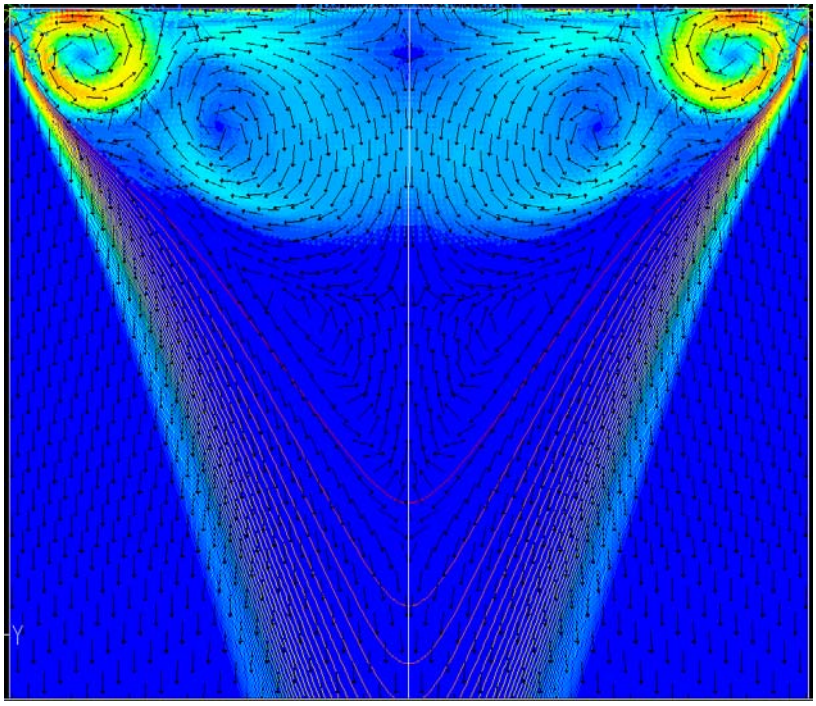

Figure 6 : Velocity field and magnitude (0-0.08 m/s) in the liquid pool

Simulations of the inclusions distribution show clearly that most of the NMI generated near (or at) the solidification front are captured by the liquid metal flow (Figure 5) . Flotation can only on a limited extend push the inclusions towards the slag. Flotation can explain why larger inclusions (9 micros) are less present in the liquid. Small inclusions follow easily the liquid flow. About 90 % of the inclusions of 9 micros finally reach the slag surface, while this proportion is only 73 % for inclusions of 2 micro diameters. The remaining inclusions are captured by the mushy region. A clear mechanical segregation towards the ingot can be observed in Figure 5. Inclusions of 9 micro are almost inexistent in the centre but very present at the ingot surface. A less strong segregation is predicted for 2 micro inclusions. The origin of this phenomenon is clearly related to the flow within the liquid pool (Figure 6). The strongest velocity magnitudes are generated by the thermal buoyancy near the mould. This strong flow propels strongly the inclusions within the mushy region, leading to an increase in inclusions number in this region.

Conclusions

The differences in the inclusion properties happen on a (sub-) microscopically small scale and can only be made clearly visible by using an electron microscope. Usual light-optical methods are not sufficient due to a lack of chemical analysis and too small enlargement and dissolution precision.

The inclusion content of ESR ingots is mainly determined by precipitation and growth processes in the liquid metal pool and in the two-phase region of the solidification front. Here, a significant decrease of the NMI proportion takes place, because the newly built particles are usually smaller than the ones in the electrode.

The frequency of the inclusions was found to decrease from the boundary towards the centre while their size increases. Simulations were performed to explore the origin of this segregation. It was shown that large inclusions are strongly expelled by the action of the flow towards the ingot surface. The numerical model can predict the trajectory of the inclusions. Inclusions that nucleate deep in the mushy region were not taken into account. This is why at the present stage it can not predict yet how many inclusions can be found in the ingot. In the future a thermodynamic model will be implemented to predict how much of alloying element will diffuse from the slag to the metal. Then a nucleation and a growth model will be used to predict the number and the sizes of the inclusions.

References

[1] Vacugov, G. A., V. V. Chlynov und G. A. Chasin: Entfernung der nichtmetallischen Einschlüsse beim Elektroschlackenumschmelzen. STAL in Deutsch (1967), 969-971.

[2] Kljuev, M. M. und V. M. Spicberg: Abscheidung und Bildung nichtmetallischer Einschlüsse im Metall beim Elektroschlacke-Umschmelzverfahren. STAL in Deutsch (1969), 590-594.

[3] Kay, D. A. R. and R. J. Pomfret: Removal of oxide inclusions during AC electroslag remelting. Journal of The Iron and Steel Institute (1971), 962-965.

[4] Mitchell, A.: Oxide inclusion behaviour during consumable electrode remelting. Ironmaking and Steelmaking (1974), 172-179.

[5] Zhengbang, Li: Mechanism of oxide inclusions removal in the ESR Process. Special Melting and Processing Technologies (1988), 732-743.

[6] Schneider, R. et al.: DESU-Prozessoptimierung zur Herstellung stickstofflegierter Stähle mit höchstem Reinheitsgrad. BHM 147 (2002), 1-6.

[7] Klujev, M. M. und Ju. M. Mironov: Über die Größe der Reaktionsfläche beim Elektroschlackenumschmelzverfahren. STAL in Deutsch (1967), 964-968.

[8] Fraser, M. E. and A., Mitchell: Mass transfer in the electroslag process: Part 1 mass-transfer coefficients. Ironmaking and Steelmaking (1976), 279-287.

[9] Povolotskii, D. Ya., V. A. Voronov und B. M. Nikitin: Removal of non-metallic inclusions during electroslag remelting. Steel in the USSR (1971), 952-954.

[10] Chan, J. C. F., J. W. Guerard and D. Miller: The re-solution of inclusions in remelted stainless steels. Metallurgical Transactions B 7B (1976), 135-141.

[11] Roshchin, V. E., et al: Transformation of non-metallic inclusions in metal of consumable electrodes during remelting. Steel in the USSR (1978), 679-681.

[12] Ueda, S., et al.: 36Ni-Fe ingot with high cleanliness with ESR prozess. Proceedings of the 15th International Forgemaster Meeting. Kobe (2003), 94-101.

[13] Nuspl, M., et al.: Qualitative and quantitative determination of micro-inclusions by automated SEM/EDX analysis. Anal. and Bioanalytical Chemistry 379, (2004), 640-645.

[14] Nadif M., C. Gatellier: Influence d´une addition de cacium ou de magnesium sur la solubilité de l´oxygéne et du soufre dans l´acier liquide. Revue de Métallurgie - CIT (1986), 377-394.

[15] Privalov N. T., V. C. Kapelnickij und N. A. Tulin: Qualitätsverbesserung bei der Stahlmarke DI-1 durch Umschmelzen nach dem ESU-Verfahren und im Vakuum-Lichtbogenofen. Stahl in Deutsch (1967), 1081-1084.

[16] Saltykov, S. A.: Stereometrische Metallographie. Deutscher Verlag Für Grundstoffindustrie, Leipzig (1974).

[17] B. E. Launder and D. B. Spalding. Lectures in Mathematical Models of Turbulence. Academic Press, London, England, 1972.

[18] S. A. Morsi and A. J. Alexander, J. Fluid Mech. 55(2) (1972) 193-208.

[19] B. J. Daly and F. H. Harlow. Phys. Fluids 13 (1970) 2634-2649.